ISSN 1674-1056
http://cpb.iphy.ac.cn
http://iopscience.iop.org/cpb
中国物理 B
Chinese Physics
中国物理
Chinese Physics B

Quantitative measurement of magnetic parameters by electron magnetic chiral dichroism

Dong-Sheng Song(宋东升), Zi-Qiang Wang(王自强), Xiao-Yan Zhong(钟虓龑), Jing Zhu(朱静)
Citation: Chin. Phys. B . 2018, 27(5): 056801. **doi:** 10.1088/1674-1056/27/5/056801

Journal homepage: http://cpb.iphy.ac.cn; http://iopscience.iop.org/cpb

What follows is a list of articles you may be interested in

Computing methods for icosahedral and symmetry-mismatch reconstruction of viruses by cryo-electron microscopy

Bin Zhu(朱彬), Lingpeng Cheng(程凌鹏), Hongrong Liu(刘红荣)
Chin. Phys. B . 2018, 27(5): 056802. **doi:** 10.1088/1674-1056/27/5/056802

TOPICAL REVIEW — Electron microscopy methods for the emergent materials and life sciences

Quantitative measurement of magnetic parameters by electron magnetic chiral dichroism

Dong-Sheng Song(宋东升)[†], Zi-Qiang Wang(王自强), Xiao-Yan Zhong(钟虓龑), and Jing Zhu(朱静)[‡]

National Center for Electron Microscopy in Beijing; Key Laboratory of Advanced Materials (MOE) and the State Key Laboratory of New Ceramics and Fine Processing, School of Materials Science and Engineering, Tsinghua University, Beijing 100084, *China*

(Received 25 January 2018; revised manuscript received 1 March 2018; published online 26 April 2018)

Electron magnetic circular dichroism opens a new door to explore magnetic properties by transmitted electrons in the transmission electron microscope. However, obtaining quantitative magnetic parameters, such as spin and orbital magnetic moment with element-specificity, goes a long way along with the development and improvement of this technique both in theoretical and experimental aspects. In this review, we will give a detailed description of the quantitative electron magnetic circular dichroism (EMCD) technique to measure magnetic parameters with spin-specificity, element-specificity, site-specificity, and orbital-spin-specificity. The discussion completely contains the procedures from raw experimental data acquisition to final magnetic parameters, together with the related custom code we have developed.

Keywords: quantitative electron magnetic circular dichroism (EMCD) technique, dynamical diffraction effects, spin and orbital magnetic moment

PACS: 68.37.Lp, 61.05.jd, 07.55.Jg **DOI:** 10.1088/1674-1056/27/5/056801

1. Introduction

The newly developed techniques in the modern advanced transmission electron microscope (TEM) aim to reach the ultimate limitation of spatial resolution and energy resolution to resolve the subtle details and fine changes of atomic structure, chemical composition, and electronic structure. However, magnetic information is usually rarely explored to keep pace with these rapid developments because of the limited magnetic characterization techniques throughout the history of this field in the TEM. Overall, several magnetic imaging techniques are involved, namely Lorentz microscopy, off-axis electron holography, and differential phase contrast.[1,2] There is no denying that they have provided plenty of magnetic information in different ways. Still, the pursuit of new techniques with much higher spatial resolution and more detailed magnetic information has never stopped though it is developing slowly.

In 2006, Schattschneider *et al.*[3] for the first time demonstrated that an electron magnetic circular dichroism (EMCD) signal can be detected in the TEM by transmitted electrons after his proposal of using electron energy-loss spectra (EELS) based on specific diffraction geometry in 2003,[4] which is reported as the EMCD technique. As a counterpart of x-ray magnetic circular dichroism (XMCD),[5,6] based on the transmitted electrons instead of the expensive synchrotron radiation source, EMCD provides the same magnetic parameters with element specificity. Paired with the complementary analytical methods for crystallographic, electronic, and chemical information at atomic scale in modern advanced TEM, EMCD has become a new powerful technique for the comprehensive study of magnetic materials at nanometer scale in recent years.

EMCD differs from previous magnetic characterization methods in the TEM as it is presented as a spectroscopy technique. It provides a new insight of magnetic measurement in the following three aspects. Firstly, it is the same as XMCD with both element specificity and spin specificity, which is an advantage comparing with these phase contrast based on magnetic imaging techniques that are bulk sensitive. The element with different spin orientation has definitely resolved a deeper understanding of magnetic behaviors. Secondly, EMCD provides intrinsic magnetic parameters, spin and orbital magnetic moment, as it can directly probe the spin characters of electrons. Note that phase contrast methods reply on the phase shift caused by magnetic potential, which is an assemble of spin electrons with interaction. Finally, the new record of spatial resolution for EMCD has just been broken from ~ 1 nm[7–9] to atomic-plane resolution by introducing the chromatic-aberration-corrected TEM[10] or using the beam-shift EMCD technique.[11] This record for the former one should be the best one among reported results for all magnetic characterization techniques in the TEM.[10] In addition, EMCD is still being developed now and new achievements have already been made, such as EMCD for polycrystalline,[12] in-plane EMCD technique,[13] and EMCD in Lorentz mode.[14,15] Along with these characteristics and advantages, one of the most challenging and attractive issues

[†]Corresponding author. E-mail: todongsheng@126.com
[‡]Corresponding author. E-mail: jzhu@mail.tsinghua.edu.cn

© 2018 Chinese Physical Society and IOP Publishing Ltd

for EMCD is to obtain reliable quantitative magnetic parameters at nanometer scale, that is the quantitative EMCD technique and the main topic of the present review.

However, EMCD is actually a complicated technique because of its electron-based detection source, additional strict requirements according to its basic principle, etc. Even so, lots of efforts have been devoted to promote the development of the EMCD technique both in theoretical and experimental aspects in past years, such as the improvements of spatial resolution and signal-noise-ratio (SNR),[7–9,16,17] the fundamental understanding of its theory[18–22] and quantitative measurements of spin and orbital magnetic moments with element-specificity and site-specificity.[23–27] Concerning the topic of this review, we summarize these issues for quantitative EMCD magnetic measurement as follows. First of all is the dynamical diffraction effects. In the periodic crystal structure, the incoming electron wave function becomes a superposition of Bloch waves, and dynamical diffraction effects become quite remarkable to affect the intensity and distribution of EMCD signal in the diffraction plane.[21,28,29] In addition, it leads to additional coefficients in the sum rules, complicating the quantitative EMCD technique.[20] As the crystal serves as a beam splitter to create the chiral EELS signal, monocrystalline of the probed area, and dynamical diffraction effects are unavoidable. The second one is the strict diffraction geometry, which is critical to provide the conjugate positions for signal acquisition. The diffraction geometry is limited to the systematical reflection condition, such as two-beam and three-beam cases, and extended to zone axis now.[30] Besides, the asymmetry of different diffraction geometries and its influence on the quantitative magnetic measurement has already been discussed, which refers to the accuracy of quantification.[23,25,31–35] The third one is the notoriously low intensity and SNR of EMCD signals. A high-quality signal leads to highly reliable quantitative measurements. Optimizing experimental conditions and improving SNR will be of significant benefit to quantitative EMCD technique. The last but not the least should be the complex and tedious data processing and signal extraction. There are some pitfalls here and much attention should be paid to minimize the errors.

In this review, we will give a detailed description of procedures on quantitative EMCD magnetic measurement, along with the custom code we have developed to simulate dynamical coefficients, process the raw data, extract intrinsic magnetic chiral dichroism signals, and calculate magnetic parameters and errors. The flowchart is displayed in Fig. 1. The example of $Y_3Fe_5O_{12}$ (YIG) is taken for demonstration here. In the second part, the theory of dynamical diffraction effects and EMCD is shortly presented to help understand the calculation principles of dynamical coefficients. In the third part, the key points for experimental signal acquisition and raw data processing are introduced to obtain initially experimental EMCD signals. In the fourth part, together with the calculated dynamical coefficients and pre-processed experimental EMCD signals, the intrinsic MCD signals free from dynamical diffraction effects are extracted. In the fifth part, the magnetic parameters with error analysis are calculated based on the sum rules. Finally, the conclusion is drawn to summarize the quantitative EMCD technique and an outlook is given.

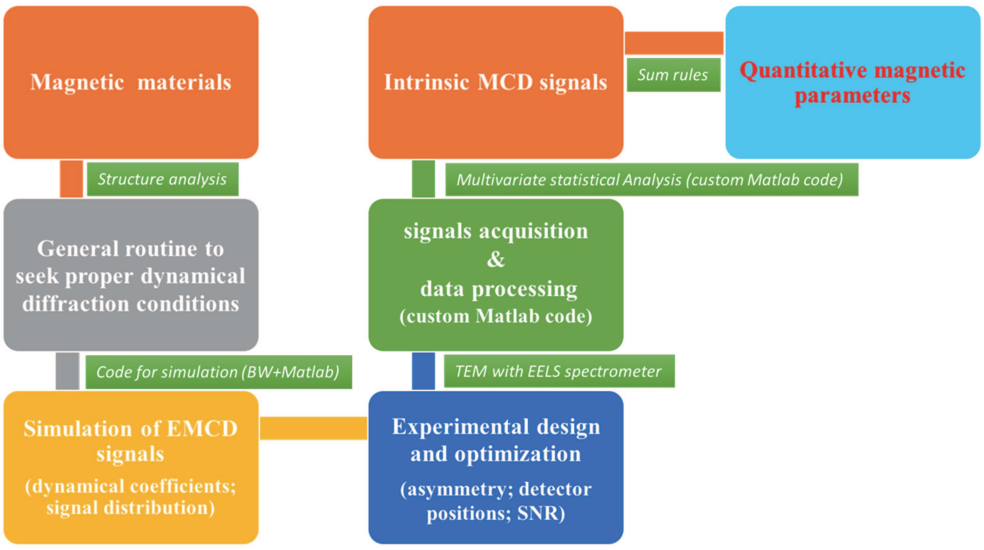


Fig. 1. (color online) The flowchart of quantitative EMCD technique.

2. Simulating dynamical coefficients

The experimental EMCD signal suffers from dynamical diffraction effects, thus the quantitative relationship between EMCD and dynamical diffraction theory should be established to calculate the dynamical coefficients for the extraction of intrinsic MCD signals. In this part, the basic theory will be introduced first. Then, the input/output parameters of the custom code for calculating dynamical coefficients will be dis-

cussed, taking the example of YIG under different experimental diffraction conditions.

2.1. Basic theory

The EMCD signal contains two EELS spectra from conjugate positons. The theory of dynamical diffraction effects and the EMCD technique has been established over the past few years. Two parts are involved: dynamical diffraction effects and mixed dynamic form factors (MDFFs). The details can be found in Refs. [18] and [19]. Based on their theory, the final double differential scattering cross-section (DDSCS) at opposite chiral positions of '+' and '–' in the diffraction plane are given by our group as follows:[24,25]

$$\begin{aligned}\left(\frac{\partial^2\sigma}{\partial E\partial\Omega}\right)_{\pm} &= \sum_u[\mu_+(E)+\mu_-(E)+\mu_0(E)]_u \\ &\times\frac{2}{3}\sum_{q,q'}\frac{q_xq'_x+q_yq'_y+q_zq'_z}{2q^2q'^2}\,\mathrm{e}^{\mathrm{i}(q-q')\cdot u}\,\mathrm{Re}(A_{q,q'}) \\ &\pm\sum_u[\mu_+(E)-\mu_-(E)]_u \\ &\times\sum_{q,q'}\frac{q_xq'_y-q_yq'_x}{2q^2q'^2}\,\mathrm{e}^{\mathrm{i}(q-q')\cdot u}\,\mathrm{Im}(A_{q,q'}), \qquad (1)\end{aligned}$$

where

$$A_{q,q'}(t)=\sum_{ghg'h'}\sum_{jlj'l'}Y^{jlj'l'}_{ghg'h'}T_{jlj'l'}(t)\delta_{q,k_\mathrm{f}+h-k_\mathrm{i}-g}\delta_{q',k_\mathrm{f}+h'-k_\mathrm{i}-g'}, \qquad (2)$$

Y is generally a product of Bloch coefficients corresponding to a certain diffraction condition, and T is a thickness dependent function. The specific expressions can be found in Refs. [17], [18], [24], and [25]. q is the momentum transfer. Variables μ_+, μ_- and μ_0 can be treated as the x-ray absorption spectra (XAS) for incident photons with left circular polarizations, right circular polarizations and linearly polarizations parallel to the wave vector direction, respectively.

Here we denote $\mu_+(E)+\mu_-(E)+\mu_0(E)$ as the isotropic signal and $\mu_+(E)-\mu_-(E)$ as the magnetic signal, which can be calculated by atomic multiplet theory[18,19] and will not be discussed here. Then, we define the terms of momentum-transfers and dynamical diffraction coefficients as the weighting factors for intrinsic signal. The simplified formula is,[25]

$$\mathrm{Spectra}_{\pm}=\frac{1}{2}\sum_u[\alpha_u(\mu_++\mu_-+\mu_0)\pm a_u(\mu_+-\mu_-)], \qquad (3)$$

where

$$\alpha_u=\frac{2}{3}\sum_{q,q'}\frac{q_xq'_x+q_yq'_y+q_zq'_z}{q^2q'^2}\,\mathrm{e}^{\mathrm{i}(q-q')\cdot u}\times\mathrm{Re}(A_{q,q'}), \qquad (4)$$

$$a_u=\sum_{q,q'}\frac{q_xq'_y-q_yq'_x}{q^2q'^2}\,\mathrm{e}^{\mathrm{i}(q-q')\cdot u}\times\mathrm{Im}(A_{q,q'}), \qquad (5)$$

u represents the coordinates of different atoms at different positions in a unit cell. α_u and a_u are the dynamical coefficients to be calculated. $\mathrm{Spectra}_+$ and $\mathrm{Spectra}_-$ are the EELS spectra acquired from the symmetric positions in the diffraction plane, respectively. The EMCD signal is the difference of the two spectra,

$$\mathrm{EMCD}=\mathrm{Spectra}_+-\mathrm{Spectra}_-=\sum_u a_u(\mu_+-\mu_-). \qquad (6)$$

2.2. Custom code for dynamical coefficients

Based on the theoretical frame described above, several kinds of software have been developed, such as the Bloch wave (BW) by Loffler *et al.*,[36] the BW + Matlab code by our group,[24,25] and also the Modified Automatic Term Selection (MATS) algorithm by Rusz *et al.*[37,38] In particular, the algorithm for MATS is optimized to avoid summation of negligible terms and to improve the calculation speed. Moreover, MATS is able to deal with the case of convergent beam, e.g., in the scanning TEM (STEM) mode,[38] rather than the assumption of plane-wave illumination in the case of BW software. Here, we will focus on the case of plane-wave illumination with our own developed Matlab code together with the BW software.

The detailed expressions of dynamical coefficients are presented in Eqs. (4) and (5), so the first step is to obtain the Bloch coefficients and momentum transfers under a certain diffraction condition for a particular crystal structure. This part is taken by the BW software, in which the input parameters can be involved in one input file and the output file contains the Bloch coefficients, elongations of the wave vector, and momentum transfers in each point-like detection position. One can refer to Ref. [36] for the software. In the input file, these following parameters are involved: crystal structure with atom positions and lattice parameters, accelerating voltage, energy loss, sample thickness, detector positions, the selected reflections being excited both for the incident and outgoing beam, and the direction of incident beam or the orientation of sample. The principle is to solve the dispersion function before and after energy loss under certain incoming and outgoing conditions. The incoming condition is determined by the orientation of crystal structure relative to incident beam. The outgoing condition is determined by the detector positions.

After that, our custom Matlab code is used to calculate dynamical coefficients based on Eqs. (4) and (5) through the summation over each atomic position. This step is time consuming with the increased number of incoming/outgoing beams, which has already been optimized in Jan's MATS algorithm. Even so, our custom code with a small amount of reflection basis can guarantee the convergence of dynamical coefficients for the systematical case, such as the two-beam or three-beam case.[26] Finally, the dynamical coefficients for nonmagnetic and magnetic components are obtained, which will be used in Section 4.

2.3. An example of YIG

To present the characters of site specificity and spin specificity for the quantitative EMCD technique, it is better to

choose the magnetic materials with the same element sited at different crystallographic positions. Here, we take YIG as an example. In addition, YIG has a very complex crystallographic and magnetic structure, and it is suitable to demonstrate the generality of the quantitative EMCD technique. YIG has a ferromagnetic and garnet structure. Yttrium ions are located at the dodecahedral sites, and iron ions are located at octahedral (oct) and tetrahedral (tet) sites, respectively. The magnetic moments of octahedral and tetrahedral Fe ions are antiparallel in alternate {111} planes. The magnetic structure can be written as $Y_3[Fe_2^{3+}, \downarrow]_{oct}[Fe_3^{3+}, \uparrow]_{tet}O_{12}$. The projection of the YIG unit cell along the [1-10] direction is shown in Fig. 2(a) (not including oxygen atoms). The EMCD signals for YIG can be expressed as

$$\begin{aligned}\text{Spectra}_{\pm} = & \frac{1}{2}[\alpha_{\text{oct}}(\mu_+ + \mu_- + \mu_0)_{\text{oct}} \\ & + \beta_{\text{tet}}(\mu_+ + \mu_- + \mu_0)_{\text{tet}}] \\ & \pm \frac{1}{2}[a_{\text{oct}}(\mu_+ - \mu_-)_{\text{oct}} + b_{\text{tet}}(\mu_+ - \mu_-)_{\text{tet}}]. \quad (7)\end{aligned}$$

Here, we choose three kinds of diffraction conditions to meet the requirement of quantitative measurement for the enhancement of Fe at octahedral and tetrahedral sties, that is, (4-44) three-beam and two-beam cases, $2\theta_B$ incident with (8-88) planes strongly excited, see Ref. [26] for details. The tilt angle is about 9.4° to reach the (4-44) three-beam case from the [1-10] zone axis. By tilting the incident beam further in the perpendicular direction by $\sim 0.3°$, the (4-44) two-beam case is obtained. The calculations are conducted under the systematic reflections with the (incident/outgoing) 5/5 beams along the reflections axis used. The accelerating voltage is set to 300 kV and the thickness is 45 nm after the optimization as shown in Fig. 2(b) at the maximum of relative intensity. The dynamical coefficients of α_{oct}, β_{tet}, a_{oct}, and b_{oct} are finally calculated for each point-like detector position in the diffraction plane under different diffraction conditions. The simulated distribution of the relative intensity of the EMCD signal under these three diffraction conditions is shown in Fig. 2(c)–2(e). The relative intensity of EMCD signals for Fe is defined with the combination of dynamical coefficients as follows:

$$\begin{aligned} I &= \frac{\text{Spectra}_+ - \text{Spectra}_-}{\text{Spectra}_+ + \text{Spectra}_-} \\ &= \frac{a_{\text{tet}}(\mu_+ - \mu_-)_{\text{tet}} - b_{\text{oct}}(\mu_+ - \mu_-)_{\text{oct}}}{\alpha_{\text{tet}}(\mu_+ + \mu_- + \mu_0)_{\text{tet}} + \beta_{\text{oct}}(\mu_+ + \mu_- + \mu_0)_{\text{oct}}} \\ &\approx \frac{a_{\text{tet}} - b_{\text{oct}}}{\alpha_{\text{tet}} + \beta_{\text{oct}}} \frac{(\mu_+ - \mu_-)_{\text{Fe}}}{(\mu_+ + \mu_- + \mu_0)_{\text{Fe}}}. \end{aligned} \quad (8)$$

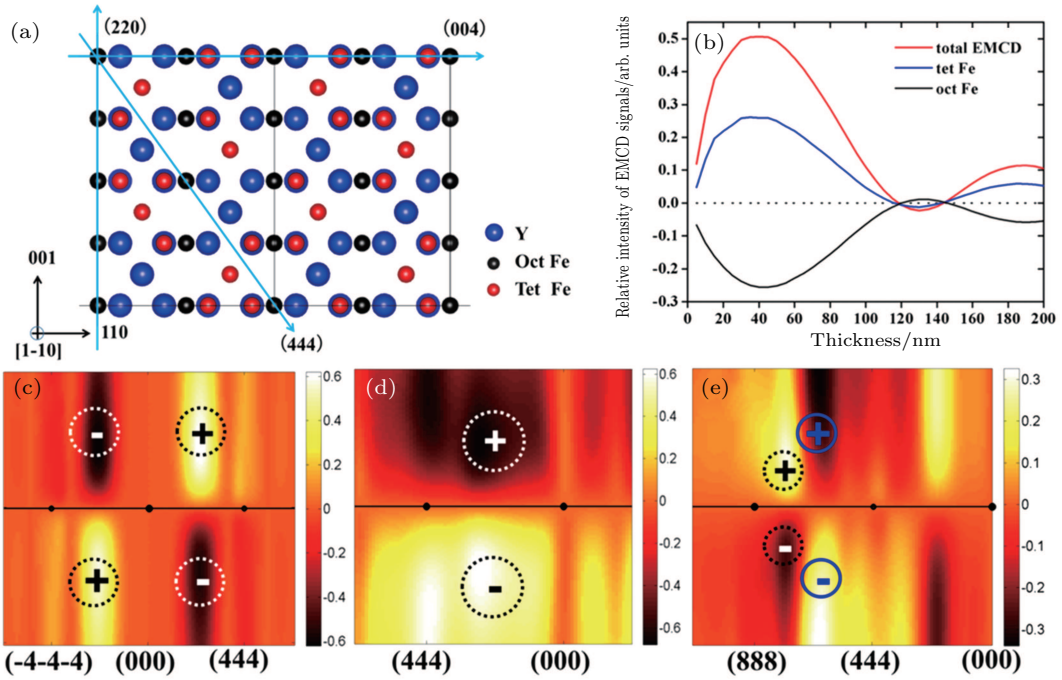


Fig. 2. (color online) Simulated dynamical coefficients of YIG. (a) Crystal structure of YIG along the [1-10] direction. (b) Simulated thickness dependent EMCD signals under (444) two-beam case. (c) and (d) Simulated EMCD signals with (4-44) planes strongly excited under two-beam and three-beam case. (e) Simulated EMCD signals with (8-88) planes strongly excited. The circles represent the detector positions with strong intensity of EMCD signals for high SNR (from Ref. [26], Figs. 1 and 2).

3. Experimental signal acquisition and data analysis

In the EMCD experiment, we take two EELSs at particular positions in the diffraction plane and the EMCD signal is the difference of these two EELS spectra. The simulated distribution of EMCD signals in the diffraction plane under certain diffraction conditions will provide a practical guide to acquire an EMCD signal with high intensity and SNR. In this part, we will talk about some key points in the EMCD experiments and data processing procedures to get EMCD signals.

3.1. Key points in experiments

EMCD is based on critical diffraction geometry, thus the accurate diffraction condition is the determinant precondition. The Kikuchi lines are firstly used to tune the orientation close to the expected orientation. For fine alignment, beam tilt is often much more effective. The diffraction pattern should be checked before and after the signal acquisition to make sure that the diffraction conditions are not changed during the experiments, which might be caused by sample drift or damage. The sample thickness plays a decisive role and the larger thickness generally will lead to a less obvious or even disappearing EMCD signal. The optimized thickness can be deduced from simulations as mentioned in Section 2. It is better to roughly estimate the thickness using the low loss EELS before EMCD measurement. The probe area with high crystallinity is necessary and the damaged or amorphous area will not conform to the standard that the crystal serves as a beam splitter.

The EMCD signals are acquired at two conjugate positions, so the detector positions are very strict. The objective aperture (OA) or entrance aperture (EA) of the gatan image filter (GIF) system can be used to select the chiral positions as shown in Fig. 3. Empirically, it is better to shift the diffraction pattern with respect to the fixed positions of OA or EA. Many guided lines are plotted on the computer screen to locate the positions accurately and quickly. It was reported[39] that a software Loopy can be used to set, store, and recall the desired detector positions within milliseconds, which will effectively help to further save the experimental time. The diffraction pattern together with detector positions should be recorded as it will be used later to extract the corresponding dynamical coefficients. The collection angle is determined both by the camera length and entrance aperture. The certain collection angle is chosen based on the simulated distribution of EMCD signals in the diffraction pattern.

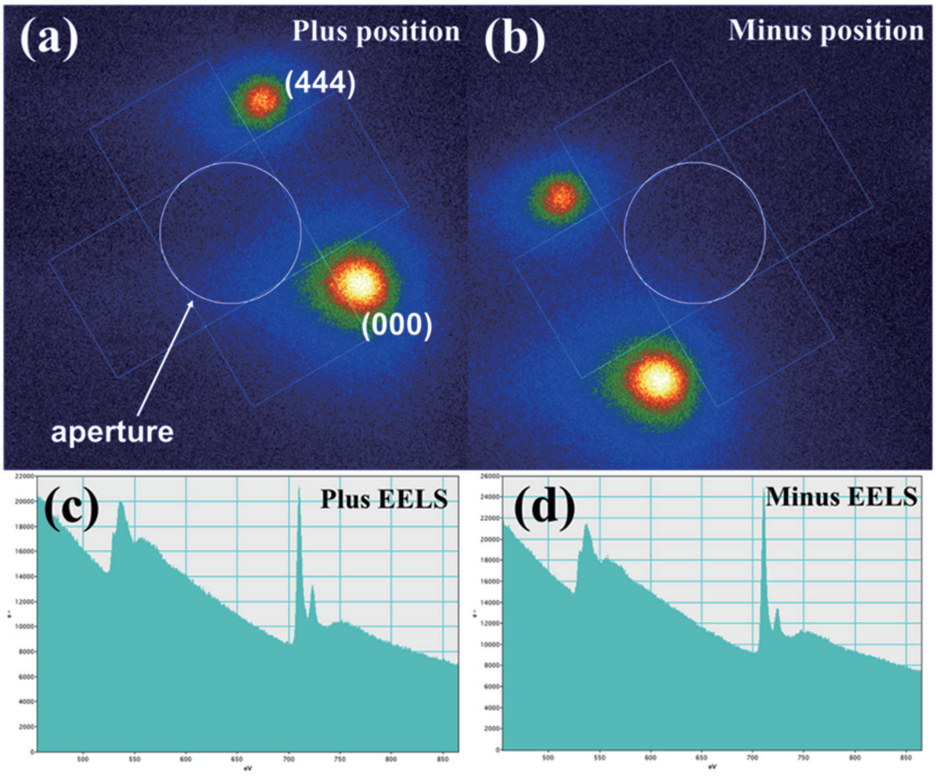


Fig. 3. (color online) Experimental setup for chiral EELS signals. (a) and (b) Energy-filtered diffraction pattern for (444) two-beam case. The white circles represent the fixed position of entrance aperture of the GIF system. The rectangles are used to locate the relative positions between entrance aperture and diffraction pattern. (c) and (d) The corresponding chiral EELS signals with the acquisition time of 5 s.

For the detector positions, the asymmetry has already been emphasized before both in the signal acquisition and quantitative measurement.[25] To meet the requirement of symmetry, the dynamical coefficients for nonmagnetic signals should be equal for the '+' and '–' positons to make sure that the nonmagnetic signals are canceled out for pure EMCD signals. Then the magnitude of asymmetry is defined as the relative error of dynamical coefficients for nonmagnetic components,

$$\text{asymmetry} = \frac{\alpha_+ - \alpha_-}{\alpha_+ + \alpha_-}, \tag{9}$$

where α_+ and α_- are the dynamical coefficients. The distribution of asymmetry for three kinds of diffraction geometry is

shown in Fig. 4 ((a) for the three-beam case, (b) for the two-beam case, and (c) for $2\theta_B$ incident). The areas with small value represent better cancelation of the nonmagnetic part and a purer EMCD signal. The detector positions with strong intensity and negligible asymmetry are selected in the experiments.

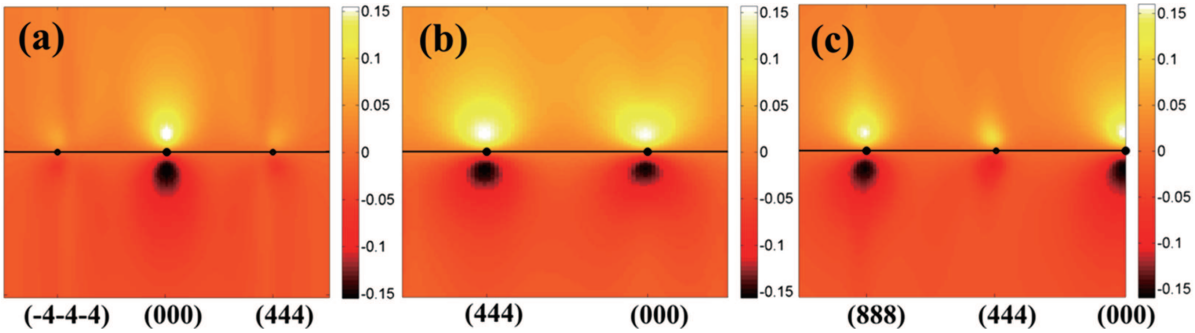


Fig. 4. (color online) Distribution of asymmetry for nonmagnetic component in the diffraction plane. (a), (b), and (c) are corresponding to the diffraction geometry of three-beam, two-beam, and $2\theta_B$ incident in Fig. 2, respectively, (from Ref. [26], Fig. S4).

3.2. Data processing for experimental EMCD signals

After the EMCD experiments, we have only got the raw data of paired EELS. First of all, energy calibration should be done for all the spectra. If the dual EELS GIF system is available, it is easy to do the calibration with respect to the low loss peak. Otherwise, the oxygen pre-edge or the onset of L_3 edge of Fe is used. After that, the following whole processing procedures are displayed in Fig. 5.

For each group of data, the plus and minus EELS should be firstly processed with pre-edge background subtraction. The backgrounds for the original EEL spectra at '+' and '–' EEL spectra are fitted in the pre-edge region following the power-law function of AE^{-r}, in which E represents the energy loss, A and r are the fitting parameters. Then the subtracted edges for the '+' and '–' spectra are shown in Fig. 5(a).

The plural scattering will also influence the measurement of magnetic parameters.[40] The removal of plural scattering for '+' and '–' background-subtracted edges is conducted in the Digital Micrograph software or our custom Matlab code using the Fourier-ratio deconvolution with a zero-loss modifier function[41] as shown in Fig. 5(b). The deconvolution is necessary as it will largely influence the relative intensity of L_2 edge when the sample is thicker, making the EMCD signals of the L_2 edge invisible. A detailed interpretation can be found in Ref. [40].

Although the '+' and '–' EELS spectra are acquired at the same conditions, such as acquisition time and collection angle, a slight variation of intensity exists and should be removed. At last, the '+' and '–' deconvoluted edges are normalized by the integration of the intensity in a post-edge window between 50 eV and 100 eV after the onset energy of the L_3 edge to against the effects of asymmetry, based on an assumption that in the post-edge region the magnetic signal is negligible and only non-magnetic spectral components remain. By subtracting the two spectra, the EMCD signal is obtained in Fig. 5(c). Smooth Spectra is not recommended for the quantitative EMCD technique as it will introduce artifacts especially when the signal is very noisy. It is beneficial to improve the SNR with the increase of data volume. The processed EMCD signals for YIG under different diffraction conditions are shown in Fig. 6.

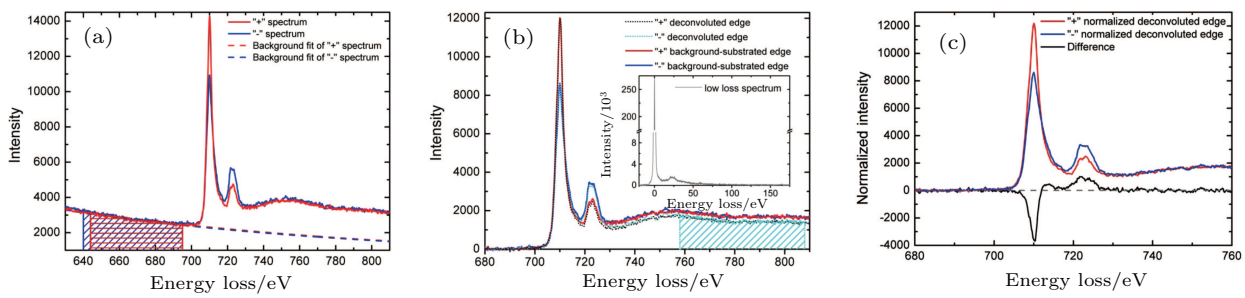


Fig. 5. (color online) Data processing procedures of EMCD spectra. (a) Pre-edge background subtraction. (b) Removal of plural scattering and post-edge normalization. (c) Experimental '+', '–', and EMCD spectra (from Ref. [24], Fig. S9).

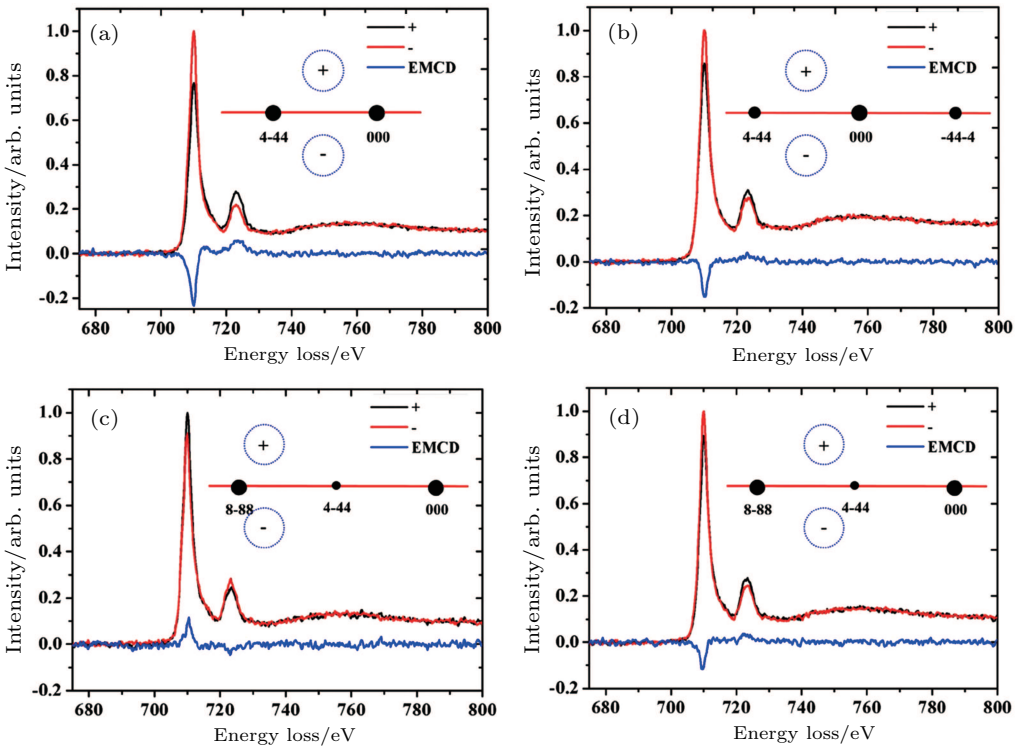


Fig. 6. (color online) Experimental EMCD signals of Fe element in YIG under different diffraction conditions. (a) and (b) are the EMCD signals from two-beam and three-beam cases, respectively. (c) and (d) are the EMCD signals with the octahedral and tetrahedral Fe enhanced under the incident angle of $2\theta_B$, respectively. The schematic drawings in each figure briefly show the diffraction geometry and the blue circles represent the positions of entrance aperture (from Ref. [26], Fig. 3).

4. Extracting intrinsic magnetic signals

The experimental EMCD signals still contain the dynamical coefficients and only the ratio of orbital and spin magnetic moment can be obtained based on the EMCD sum rules. To extract the intrinsic MCD signals for spin and orbital magnetic moment separately, the further processing is necessary. In addition, due to the low SNR of EMCD signals, plenty of datasets should be taken to improve the accuracy of quantitative magnetic measurement. The lowest SNR and standard of data volume are not evaluated here. This is because the experiments here are conducted in the TEM mode. The line or area scanning of EMCD signals in the STEM mode is required to discuss these issues, in which case the signals with different SNR can be extracted from the datasets. This part should be quantitatively discussed in the future. Therefore, normalization of all datasets and statistical methods are introduced in this part.

4.1. Normalization

A series of experimental EMCD spectra will be acquired with different intensities at different positions. It is obvious that signals with different intensities will lead to an inconsistent SNR. Therefore, it is better to keep the total intensity at the same level. To put them together the normalization is needed. Note that the normalization here is different from the post edge normalization for EMCD signals above. Based on Eq. (7), the experimental isotropic spectra $(\text{Spectra}_+ + \text{Spectra}_-)_i$ and EMCD spectra $(\text{Spectra}_+ - \text{Spectra}_-)_i$ are deduced as follows,

$$\begin{aligned}&(\text{Spectra}_+ + \text{Spectra}_-)_i \\ &= w_i[\alpha_i(\mu_+ + \mu_- + \mu_0)_{\text{oct,Fe}} + \beta_i(\mu_+ + \mu_- + \mu_0)_{\text{tet,Fe}}], \quad (10)\\ &(\text{Spectra}_+ - \text{Spectra}_-)_i \\ &= w_i[a_i(\mu_+ - \mu_-)_{\text{oct,Fe}} + b_i(\mu_+ - \mu_-)_{\text{tet,Fe}}], \quad (11)\end{aligned}$$

where w_i is the parameter related to an individual EMCD experimental measurement, which should be normalized among different measurements. By integrating Eq. (10) over the L_3 and L_2 edge of Fe,

$$\begin{aligned}N_i &= \int_{L_2+L_3} (\text{Spectra}_+ + \text{Spectra}_-)_i \,\mathrm{d}E \\ &= w_i(\alpha_i + \beta_i) \int_{L_2+L_3} (\mu_+ + \mu_- + \mu_0)_{\text{Fe}} \,\mathrm{d}E. \quad (12)\end{aligned}$$

The normalization factor w_i is expressed as

$$w_i = \frac{N_i}{(\alpha_i + \beta_i)\int (\mu_+ + \mu_- + \mu_0)_{\text{Fe}} \,\mathrm{d}E}. \quad (13)$$

For each group, the integration over a certain energy range for $(\text{Spectra}_+ + \text{Spectra}_-)_i$ (N_i) can be calculated after the removal of fitted background with a double step function. At last, by substituting Eqs. (12) and (13) to Eq. (11), the final EMCD signals are expressed as,

$$(\text{Spectra}_+ - \text{Spectra}_-)_i$$

$$= \frac{N_i a_i}{\alpha_i + \beta_i} \frac{(\mu_+ - \mu_-)_{\text{oct,Fe}}}{\int\limits_{L_2+L_3} (\mu_+ + \mu_- + \mu_0)_{\text{oct,Fe}}} + \frac{N_i b_i}{\alpha_i + \beta_i} \frac{(\mu_+ - \mu_-)_{\text{tet,Fe}}}{\int\limits_{L_2+L_3} (\mu_+ + \mu_- + \mu_0)_{\text{tet,Fe}}}. \quad (14)$$

(Spectra$_+$ − Spectra$_-$) are the processed EMCD signals in Section 3. N_i is the integration of isotropic signal. Along with the calculated dynamical coefficients in Section 2, the required parameters in Eq. (14) are all determined. The intrinsic isotropic signal is still involved in the formula as it also appears in the sum rules (see below). The dynamical coefficients (including isotropic and anisotropic) here together with the normalization factors become the new weighting factors. Note that the dynamical coefficients here are obtained by averaging all the values falling into the detector. Our custom Matlab code is able to conduct this step by correlating the detector positions in the experimental diffraction plane with simulated distributions, in which the positions of diffraction spots and diameter of aperture should be provided. These data can be manually extracted from the recorded experimental diffraction pattern in Section 3. The mesh grid for the diffraction plane in the simulation is usually set at 0.2–0.25 mrad per pixel to guarantee the accuracy and calculation speed.

4.2. Least square fitting for intrinsic signals

The matrix form of Eq. (14) can be written as[24,42]

$$\boldsymbol{D} = \boldsymbol{W}\boldsymbol{S}^{\mathrm{T}} + \boldsymbol{E}, \quad (15)$$

where

$$W = \begin{pmatrix} \frac{a_{\text{oct1}}}{\alpha_{\text{oct1}} + \beta_{\text{tet1}}} & \frac{b_{\text{tet1}}}{\alpha_{\text{oct1}} + \beta_{\text{tet1}}} \\ \cdots & \cdots \\ \frac{a_{\text{octN}}}{\alpha_{\text{octN}} + \beta_{\text{tetN}}} & \frac{b_{\text{tetN}}}{\alpha_{\text{octN}} + \beta_{\text{tetN}}} \end{pmatrix},$$

N is the number of spectra. The matrix $\boldsymbol{D}$ represents the experimental dataset of EMCD spectra divided by normalization factor N_i. The matrix $\boldsymbol{S}$ represents the intrinsic MCD signal of octahedral and tetrahedral Fe. The matrix $\boldsymbol{W}$ is composed of weighting factors, and $\boldsymbol{E}$ denotes the residual. Through the least square fitting method, the optimal matrix $\boldsymbol{S}^{\mathrm{T}}$ can be solved by fitting the experimental data matrix $\boldsymbol{D}$ to the best level for which the sum of the square of the elements in matrix $\boldsymbol{E}$ is minimized. The optimal solution is $\boldsymbol{S}^{\mathrm{T}} = (\boldsymbol{W}^{\mathrm{T}}\boldsymbol{W})^{-1}(\boldsymbol{W}^{\mathrm{T}}\boldsymbol{D})$. The intrinsic MCD signals for octahedral and tetrahedral Fe of YIG are shown in Fig. 7. The opposite sign of EMCD signals for octahedral and tetrahedral Fe indicates the antiferromagnetic coupling between them. For crystal structure with only one crystallographic site, the case becomes much more simple.

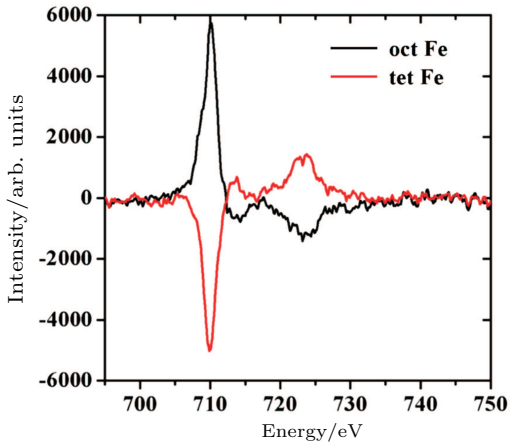


Fig. 7. (color online) Intrinsic EMCD signals for octahedral (black) and tetrahedral (red) Fe of YIG (from Ref. [24], Fig. 4).

5. Magnetic parameters and error analysis

Now the intrinsic MCD signals free from dynamical diffraction effects are obtained, similar to the XMCD signals. Therefore, it is ready to apply the sum rules for magnetic parameters.

5.1. Sum rules

Here, we will talk about the sum rules first. The XMCD technique has its own sum rules to get quantitative magnetic parameters based on the experimental spectra,[43,44] while it is not entirely suitable to EMCD, for which the dynamical diffraction effects should be taken. In 2007, the analytical form of sum rules for EMCD is derived and the quantitative magnetic parameters, the ratio of spin, and the orbital moment for the magnetic element are obtained after applying it to experimental results.[20,21] The formula of EMCD sum rules is similar to XMCD sum rules. However, it should be noted that the orbital and spin magnetic moments are expressed explicitly in terms of both experimental spectra and dynamical diffraction coefficients, which is not the same case in XMCD. The sum rules used here are the formula of XMCD (Eqs. (16) and (17)). This is because the intrinsic signals are free from dynamical diffraction effects. The contribution of the magnetic-dipole operator $\langle T_z \rangle$ can be neglected for 3d metal. The integration energy ranges are 704 eV–717 eV for the Fe L_3 edge, and 717 eV–731 eV for the Fe L_2 edge here. The n_{h} values for oct Fe and tet Fe are both chosen as 5 due to their $3d^5$ electronic configurations, which is just an approximation value.

$$\frac{\int\limits_{L_3} (\mu_+ - \mu_-)\,\mathrm{d}E + \int\limits_{L_2} (\mu_+ - \mu_-)\,\mathrm{d}E}{\int\limits_{L_{2,3}} (\mu_+ + \mu_- + \mu_0)\,\mathrm{d}E} = \frac{\langle L_z \rangle}{2n_h}, \quad (16)$$

$$\frac{\int\limits_{L_3} (\mu_+ - \mu_-)\,\mathrm{d}E - 2\int\limits_{L_2} (\mu_+ - \mu_-)\,\mathrm{d}E}{\int\limits_{L_{2,3}} (\mu_+ + \mu_- + \mu_0)\,\mathrm{d}E} = \frac{2\langle S_z \rangle}{3n_h} + \frac{7\langle T_z \rangle}{3n_h}, \quad (17)$$

where $\langle S_z \rangle$, $\langle L_z \rangle$, $\langle T_z \rangle$ are respectively the ground-state ex-

pectation values of spin momentum, orbital momentum, and magnetic-dipole operators. n_h is the number of d holes.

Applying the sum rules to the intrinsic MCD signals, the magnetic parameters of YIG are obtained as listed in Table 1. It is always better to compare some of these magnetic parameters with those from other techniques, which might help to evaluate the accuracy of the EMCD technique. In contrast, the EMCD technique not only shows the capability of solving magnetic structures, such as the ferromagnetic structure of YIG, it also achieves very comprehensive magnetic information. The characteristics, spin specificity, site specificity, element specificity, and orbital-spin-moment specificity are all demonstrated here, which cannot be achieved by any single magnetic characterization technique.

Table 1. Magnetic parameters of YIG.

Magnetic parameters	EMCD	Neutron diffraction	First principle calculation	Macro measurement
m_L/m_S (oct)	0.06±0.02			
m_L/m_S (tet)	0.08±0.02			
m_L(oct)	0.28±0.03			
m_L (tet)	0.31±0.03			
m_S (oct)	4.5±0.2			
m_S (tet)	3.9±0.2			
M_{oct}	4.8±0.2		4.12	
M_{tet}	4.2±0.3		4.20	
M_{total} (unit cell)	3.0±0.7	3.1	4.36	3.3

Note: m_L/m_S refers to the ratio of orbital and spin magnetic moment (m_L is the orbital magnetic moment and m_S is the spin magnetic moment). M_{oct} and M_{tet} are the total atomic magnetic moments (including the orbital and spin magnetic moment) of oct and tet Fe in the units of μ_B per atom. M_{total} is the total magnetic moment for $Y_3Fe_5O_{12}$ in a unit cell. (from Ref. [26], Table 1).

5.2. Error analysis

The error analysis is necessary to evaluate the reliability of quantitative measurement and the error bars from different sources are given to help understand and improve the accuracy of the quantitative EMCD technique. The estimation of these errors involves the deviations from data pre-processing, the noise in EMCD spectra, the measurement of sample thickness, and the calculations of theoretically obtained dynamical coefficients. The total error is obtained by adding them together. We will give a respective discussion in the following.

For the data pre-processing, we have used different pre-edge windows, low-loss spectra and normalization regions in each step as discussed in section 3. It turns out that the errors from data processing, including pre-edge background subtraction, removal of plural scattering, and post-edge normalizing, are very small and their contributions are all negligible. Therefore, the details are not presented here. The reason is that the SNR for chiral EELS here is relatively high. The high counts and thin sample in the EMCD experiment in the TEM mode lead to a high signal-background ratio and weak multiple scattering. However, this part should be re-considered if the SNRs of EELS signals are very low, such as in the STEM mode or others.

For the noise in EMCD spectra, the standard errors for the magnetic parameters are calculated from a series of independent pairs of EMCD spectra as shown in Table 2. The total error of m_L/m_S is almost totally contributed by this term, showing the great importance of SNR for the quantitative EMCD technique. Therefore, it is always helpful to obtain the m_L/m_S from a large amount of data, such as in the EFDIF (energy filtered diffraction) mode or STEM mode reported in Refs. [8], [23], and [45]. Besides, the SNR also leads to a large error of magnetic moments.

The measurement error of sample thickness is about ±1.7 nm determined by convergent beam electron diffraction (CBED) and low-loss EELS. The dynamical coefficients corresponding to the thickness varying from 45.0 nm to 48.4 nm ($t = 46.7$ nm) are calculated to give the error. However, its influence on magnetic parameters is negligible, for the change of dynamical coefficients in this range of thickness is very flat as shown in Fig. 2(b).

The error of dynamical coefficients is difficult to be evaluated. The possible uncertainties in the imprecise knowledge of experimental dynamical diffraction conditions will undoubtedly contribute to the error of magnetic parameters. These factors, such as the orientation of sample, detector positions, convergence and collection angle, tilt angle from zone axis, partial coherence of the incident beam, and the defects of the sample, will contribute to the uncertainty of dynamical coefficients, while only some of them can be determined currently. For example, the estimation for the positons of detector and tilt angle is done here. The center of the detector is moved to right and left with $0.1G_{4-44}$ along the systematic row with a diameter of $0.5G_{4-44}$ under the two-beam case during the calculations, which is close to the position of the collection aperture in the experiments. The change of dynamical diffraction coefficients is less than about 6.5%. For the tilt angle from the [1-10] zone axis, we take the angles of 8.4°, 9.4°, and 10.4° respectively to calculate the dynamical coefficients and the variation is less than 3%. Therefore, the actual error should be larger than 9.5%. However, the exact value is actually unknown. As they all have an effect on the dynamical coefficients during the quantitative measurement, we finally use the 20% random error of dynamical coefficients to estimate it (errors in Table 2 take this case). Meanwhile, the random noise with maximum of ±10% and ±5% are also used to estimate the errors as shown in Table 3 for comparison. It is found that the errors for magnetic parameters are very sensitive to the value of random noise, especially the total magnetic moment.

Table 2. Errors of different sources (from Ref. [26], Table S1).

Error source	m_L/m_S (oct Fe)	m_L/m_S (tet Fe)	$M_{oct,Fe}$	$M_{tet,Fe}$	M_{total}/unit cell
Noise	0.021	0.017	0.11	0.15	0.33
Thickness	0.000	0.000	0.01	0.01	0.04
Dynamical coefficients (20%)	0.003	0.004	0.15	0.18	0.65
Total error (20%)	0.021	0.018	0.19	0.24	0.73
Calculated value	0.06	0.08	4.8	4.2	3.0

Table 3. Errors of dynamical coefficients with different random noise (from Ref. [26], Table S2).

Error sources	m_L/m_S (oct Fe)	m_L/m_S (tet Fe)	$M_{oct,Fe}$	$M_{tet,Fe}$	M_{total}/unit cell
Dynamical coefficients (20%)	0.003	0.004	0.15	0.18	0.65
Dynamical coefficients (10%)	0.001	0.001	0.11	0.07	0.27
Dynamical coefficients (5%)	0.001	0.001	0.05	0.02	0.10
Total error (20%)	0.021	0.018	0.19	0.24	0.73
Total error (10%)	0.021	0.017	0.15	0.17	0.43
Total error (5%)	0.021	0.017	0.12	0.15	0.35
Calculated value	0.06	0.08	4.8	4.2	3.0

That is to say, the quantitative EMCD technique is heavily dependent on the simulation of dynamical diffraction effects. It is obvious that the calculation of dynamical coefficients is very complicated. Then it is impossible to obtain accurate dynamical coefficients due to the uncertainty discussed above. Therefore, advanced statistical methods with specific physical significance and boundary conditions, such as the multivariate curve resolution (MCR)[35,42,46] that has already been tested, should be developed or combined together to solve these problems for further development of quantitative EMCD technique in the future.

6. Conclusion and outlook

In this review, the detailed procedures for the quantitative EMCD technique are presented taking the example of YIG. The whole process can be summarized as follows: acquiring experimental chiral EELS signals and pre-processing for EMCD signals, simulating dynamical coefficients, extracting intrinsic MCD signals, calculating magnetic parameters and error analysis. The related custom code (QEMCD, quantitative EMCD)[47] can be divided into two parts: simulating dynamical diffraction effects by BW software and custom Matlab code, and extracting intrinsic signals and magnetic parameters by custom Matlab code, which can be required from the corresponding author Dong-Sheng Song. The magnetic parameters, orbital and spin magnetic moment with spin specificity, element specificity, site specificity, and orbital spin specificity can finally be measured for magnetic materials with different crystallographic structures.

However, there are still some issues of the quantitative EMCD technique that should be addressed. The first one is the low intensity and SNR of EMCD signals though it has already been optimized by simulating the dynamical diffraction effects. With the XFEG electron gun and K2 camera with direct electron detection installed on the EELS spectrometer,[47,48] the SNR can be further greatly improved with extremely increased source brightness and detection efficiency. Under the current experimental conditions, the smallest total magnetic moment per atom that has been quantitatively measured is $0.5\mu_B$ to our best knowledge in the literature.[27] To improve the detection sensitivity, the SNR and data volume are important. The lower limit should be the error of magnetic moment, which approaches $0.2\mu_B$ in Table 1. For fixed SNR, the increased data volume might be helpful to reduce the errors, thus the detection sensitivity. However, the actual lower limit of detect sensitivity for the quantitative EMCD technique is still unknown, which should be explored in the future. The second one is that the spatial resolution here is around 50 nm limited by the diameter of electron beam in the TEM mode. The spatial resolution is determined by the experimental setup, which is around 1 nm in the STEM mode[8] and ~ 0.4 nm in the chromatic-aberration-corrected TEM mode.[10] However, none of them have achieved the quantitative magnetic measurement as shown in this review. For the STEM mode, the increased complexity of dynamical diffraction effects makes dynamical coefficients much more uncertain. For atomic-plane-resolved EMCD, the intensity and SNR are still low even with the acquisition time of almost one hundred seconds. It is supposed that these problems will be solved in the immediate future with newly advanced facilities. The third problem is that the quantitative EMCD technique is only available to materials with collinearly magnetic structure. That is to say, it provides the averaged magnetic parameters of the probe area. For these non-collinearly complex magnetic systems, such as helix or spin frustration, the magnetic moment varies in the real space. Therefore, new methods need to be developed to cope with it and much more rich magnetic information will be obtained to understand the underlying mechanism of magnetic behaviors from a new insight simultaneously.

References

[1] McCartney M R and Smith D J 2007 *Annu. Rev. Mater. Res.* **37** 729
[2] Midgley P A and Dunin-Borkowski R E 2009 *Nat. Mater.* **8** 271
[3] Schattschneider P, Rubino S, Hébert C, Rusz J, Kuneš J, Novák P, Carlino E, Fabrizioli M, Panaccione G and Rossi G 2006 *Nature* **441** 486
[4] Hébert C and Schattschneider P 2003 *Ultramicroscopy* **96** 463
[5] van der Laan G and Figueroa A I 2014 *Coord. Chem. Rev.* **95** 277
[6] Fischer P 2008 *IEEE Trans. Magn.* **44** 1900
[7] Schattschneider P, Stöger-Pollach M, Rubino S, Sperl M, Hurm C, Zweck J and Rusz J 2008 *Phys. Rev. B* **78** 104413
[8] Thersleff T, Rusz J, Hjörvarsson B and Leifer K 2016 *Phys. Rev. B* **94** 134430
[9] Song D, Ma L, Zhou S and Zhu J 2015 *Appl. Phys. Lett.* **107** 042401
[10] Wang Z, Tavabi A., Jin L, Rusz J, Tyutyunnikov D, Jiang H, Moritomo Y, Mayer J, Dunin-Borkowski R, Yu R, Zhu J and Zhong X 2018 *Nat. Mater.* **17** 221
[11] Rusz J, Muto S, Spiegelberg J, Adam R, Tatsumi K, Bürgler D E, Oppeneer P M and Schneider C M 2016 *Nat. Commun.* **7** 12672
[12] Muto S, Rusz J, Tatsumi K, Adam R, Arai S, Kocevski V, Oppeneer P M, Bürgler D E and Schneider C M 2014 *Nat. Commun.* **5** 3138
[13] Song D, Tavabi A H, Li Z A, Kovács A, Rusz J, Huang W, Richter G, Dunin-Borkowski R E and Zhu J 2017 *Nat. Commun.* **8** 15348
[14] Zhang Z H, Wang X, Xu J B, Muller S, Ronning C and Li Q 2009 *Nat. Nanotechnol.* **4** 523
[15] Che R C, Liang C Y, He X, Liu H H and Duan X F 2011 *Sci. Technol. Adv. Mater.* **12** 025004
[16] Schattschneider P, Hébert C, Rubino S, Stöger-Pollach M, Rusz J and Novák P 2008 *Ultramicroscopy* **108** 433
[17] Warot-Fonrose B, Houdellier F, Hÿtch M J, Calmels L, Serin V and Snoeck E 2008 *Ultramicroscopy* **108** 393
[18] Rusz J, Rubino S and Schattschneider P 2007 *Phys. Rev. B* **75** 214425
[19] Calmels L and Rusz J 2010 *Ultramicroscopy* **110** 1042
[20] Calmels L, Houdellier F, Warot-Fonrose B, Gatel C, Hÿtch M J, Serin V, Snoeck E and Schattschneider P 2007 *Phys. Rev. B* **76** 060409
[21] Rusz J, Eriksson O, Novák P and Oppeneer P M 2007 *Phys. Rev. B* **76** 060408
[22] Rusz J, Rubino S, Eriksson O, Oppeneer P M and Leifer K 2011 *Phys. Rev. B* **84** 064444
[23] Lidbaum H, Rusz J, Liebig A, Hjörvarsson B, Oppeneer P M, Coronel E, Eriksson O and Leifer K 2009 *Phys. Rev. Lett.* **102** 037201
[24] Wang Z Q, Zhong X Y, Yu R, Cheng Z Y and Zhu J 2013 *Nat. Commun.* **4** 1395
[25] Song D, Wang Z and Zhu J 2015 *Ultramicroscopy* **148** 42
[26] Song D, Li G, Cai J and Zhu J 2016 *Sci. Rep.* **6** 18489
[27] Li G, Song D, Li Z P and Zhu J 2016 *Appl. Phys. Lett.* **108** 242414
[28] Calmels L and Rusz J 2011 *J. Appl. Phys.* **109** 07D328
[29] Rubino S, Schattschneider P, Rusz J, Verbeeck J and Leifer K 2010 *J. Phys. Appl. Phys.* **43** 474005
[30] Song D, Rusz J, Cai J and Zhu J 2016 *Ultramicroscopy* **169** 44
[31] Lidbaum H, Rusz J, Rubino S, Liebig A, Hjörvarsson B, Oppeneer P M, Eriksson O and Leifer K 2010 *Ultramicroscopy* **110** 1380
[32] Rusz J, Oppeneer P M, Lidbaum H, Rubino S and Leifer K 2010 *J. Microsc.* **237** 465
[33] Rusz J, 2009 arXiv:0910.3849
[34] Rusz J, Lidbaum H, Liebig A, Hjörvarsson B, Oppeneer P M, Rubino S, Eriksson O and Leifer K 2010 *J. Magn. Magn. Mater.* **322** 1478
[35] Muto S, Tatsumi K and Rusz J 2013 *Ultramicroscopy* **125** 89
[36] Löffler S and Schattschneider P 2010 *Ultramicroscopy* **110** 831
[37] Rusz J, Muto S and Tatsumi K 2013 *Ultramicroscopy* **125** 81
[38] Rusz J 2017 *Ultramicroscopy* **177** 20
[39] Schneider S, Pohl D, Löffler S, Rusz J, Kasinathan D, Schattschneider P, Schultz L and Rellinghaus B 2016 *Ultramicroscopy* **171** 186
[40] Rusz J, Lidbaum H, Rubino S, Hjörvarsson B, Oppeneer P, Eriksson O and Leifer K 2011 *Phys. Rev. B* **83** 132402
[41] Egerton R 2011 *Electron Energy-loss Spectroscopy in the Electron Microscope*. (Springer Science & Business Media)
[42] Tatsumi K, Muto S, Nishida I and Rusz J 2010 *Appl. Phys. Lett.* **96** 201911
[43] O'Brien W L and Tonner B P 1994 *Phys. Rev. B* **50** 12672
[44] C arra P, Thole B T, Altarelli M and Wang X 1993 *Phys. Rev. Lett.* **70** 694
[45] Thersleff T, Muto S, Werwiński M, Spiegelberg J, Kvashnin Y, Hjörvarsson B, Eriksson O, Rusz J and Leifer K 2017 *Sci. Rep.* **7** 44802
[46] Tatsumi K, Muto S and Rusz J 2013 *Microsc. Microanal.* **19** 1586
[47] Hart J L, Lang A C, Leff A C, Longo P, Trevor C, Twesten R D and Taheri M L 2017 *Sci. Rep.* **7** 8243
[48] Clough R N, Moldovan G and Kirkland A I 2014 *J. Phys. Conf. Ser.* **522** 012046